Spitzer 3.6μm and 4.5μm full-orbit lightcurves of WASP-18

P.F.L. Maxted[1], D.R. Anderson[1], A. P. Doyle[1], M. Gillon[2], J. Harrington[3],
N. Iro[1], E. Jehin[2], D. Lafrenière[4], B. Smalley[1], J. Southworth[1]

[1] *Astrophysics Group, Keele University, Keele, Staffordshire ST5 5BG*
[2] *Institut d'Astrophysique et de Géophysique, Université de Liège, Allée du 6 Août 17, Bat. B5C, 4000 Liège, Belgium*
[3] *Planetary Sciences Group, Department of Physics, University of Central Florida, Orlando, FL 32816-2385, USA*
[4] *Département de physique, Université de Montréal, C.P. 6128 Succ. Centre-Ville, Montréal, QC, H3C 3J7, Canada*

ABSTRACT

We present new lightcurves of the massive hot Jupiter system WASP-18 obtained with the Spitzer spacecraft covering the entire orbit at 3.6 μm and 4.5 μm. These lightcurves are used to measure the amplitude, shape and phase of the thermal phase effect for WASP-18 b. We find that our results for the thermal phase effect are limited to an accuracy of about 0.01 per cent by systematic noise sources of unknown origin. At this level of accuracy we find that the thermal phase effect has a peak-to-peak amplitude approximately equal to the secondary eclipse depth, has a sinusoidal shape and that the maximum brightness occurs at the same phase as mid-occultation to within about 5 degrees at 3.6 μm and to within about 10 degrees at 4.5 μm. The shape and amplitude of the thermal phase curve imply very low levels of heat redistribution within the atmosphere of the planet. We also perform a separate analysis to determine the system geometry by fitting a lightcurve model to the data covering the occultation and the transit. The secondary eclipse depths we measure at 3.6 μm and 4.5 μm are in good agreement with previous measurements and imply a very low albedo for WASP-18 b. The parameters of the system (masses, radii, etc.) derived from our analysis are in also good agreement with those from previous studies, but with improved precision. We use new high-resolution imaging and published limits on the rate of change of the mean radial velocity to check for the presence of any faint companion stars that may affect our results. We find that there is unlikely to be any significant contribution to the flux at Spitzer wavelengths from a stellar companion to WASP-18. We find that there is no evidence for variations in the times of eclipse from a linear ephemeris greater than about 100 seconds over 3 years.

Key words: stars: individual: WASP-18; planetary systems

1 INTRODUCTION

Hot Jupiters are currently at the forefront of observational studies that can provide meaningful tests for models of exoplanet atmospheres. The atmospheric temperatures for a typical hot Jupiter orbiting a solar-type star with a period of 3 days can be up to 1500 K. For transiting hot Jupiters this makes it feasible to measure the planet-star flux ratio directly from the depth of secondary eclipse in the lightcurve due to the occultation of the exoplanet by the host star. Early results with the Spitzer Space Telescope confirmed the existence of secondary eclipses in the lightcurves of HD 209458 (Deming et al. 2005) and TrES-1 (Charbonneau et al. 2005) with the expected depth $\sim$ 0.5 per cent at mid-infrared wavelengths. The secondary eclipse depth has now been measured using Spitzer for more

than 20 hot Jupiters (Cowan & Agol 2011). Comparison of these observations with atmospheric models has been used to reveal the diversity of hot Jupiter atmospheres with regard to their composition (Madhusudhan et al. 2011), the presence or absence of a temperature inversion in their atmospheres, (Knutson et al. 2010), and their albedos and heat recirculation efficiencies (Cowan & Agol 2011).

The secondary eclipse depth for a hot Jupiter at infrared wavelengths measures the brightness temperature of the hemisphere facing the star – the "day-side" – integrated over the visible hemisphere. This brightness temperature, $T_{\rm day}$, will depend on the pattern of emission over the day side, the spectral energy distribution (SED) of this emission, the Bond Albedo, A_b, and the efficiency with which heat is redistributed to the night-side of the planet. Observations at several wavelengths, particularly near-infrared observations

near the peak of the day-side SED, reduce the extent to which we must rely on models to account for the conversion from brightness temperature to effective temperature when interpreting these observations (Madhusudhan et al. 2011). In general, it is not possible to disentangle the degeneracy between Bond albedo and heat recirculation efficiencies from secondary eclipse observations alone. One exception is the case of HD 189733, in which very high quality Spitzer observations of the secondary eclipse reveal asymmetries that can be inverted to produce a map of the brightness temperature on the day side of HD 189733 b (Majeau et al. 2012; de Wit et al. 2012). Apart from this exceptional case, it is currently only possible to obtain information on the redistribution of heat in the planet's atmosphere by observing the thermal phase effect – the variation in infrared brightness of the system as a function of orbital phase.

There are several different ways to parametrize the redistribution of heat from the day-side to the night-side of a planet (Spiegel & Burrows 2010). Here we use the parameter P_n, the fraction of the incident energy that is transported to the night side of the planet. Plausible values of this parameter vary from 0 up to 0.5. A value of $P_n = 0$ would imply a night-side brightness temperature $T_{\text{night}} \ll T_{\text{day}}$, whereas $P_n = 0.5$ implies $T_{\text{night}} \approx T_{\text{day}}$.[1] If $P_n > 0$ then this suggests that winds at some level in the atmosphere move heat around the planet. In practise, very high efficiencies for strongly irradiated planets are unlikely because the winds that transport heat to the night-side will dissipate some of their energy through turbulence or shocks (Goodman 2009). Nevertheless, some redistribution of energy from the day-side to the night-side is likely, and may lead to significant offsets between the sub-stellar point and the hottest regions of the atmosphere (Cooper & Showman 2005). This will be observed in the thermal phase effect as an offset in the phase of maximum brightness from opposition.

Cowan et al. (2007) used 8 separate observations with Spitzer spread throughout the orbit of the three hot Jupiter systems HD 209458, HD 179949 and 51 Peg to measure their thermal phase effect. They were able to place useful upper limits on the phase variation in 51 Peg and HD 209458 and to detect a variation with a peak-to-trough amplitude of 0.14 per cent in HD 179949. HD 179949 is a non-transiting hot Jupiter, so the inclination of the orbit and the radius of the planet are unknown, but even allowing for this uncertainty, the observed amplitude of the phase variation provided an upper limit of $P_n < 0.21$ and shows that the hottest point is near the sub-stellar point. HD 209458 is a transiting system, so the inclination of the orbit and the radius of the exoplanet are known. This allowed Cowan et al. to translate the upper limit on the amplitude of the thermal phase into a lower limit $P_n > 0.32$, and thus establish that apparently different hot Jupiters are likely to have a variety of P_n values.

Harrington et al. (2006) detected the phase variation of the planet υ And b using the MIPS instrument on Spitzer at 24μm. With additional data and an improved understanding of the systematic noise sources in MIPS, they were able to refine their estimate of the amplitude of the phase vari-

ation and show that there is a large ($\sim 80°$) phase offset between the time of maximum brightness and opposition (Crossfield et al. 2010). The inclination and radius of υ And b are not known accurately because it is a non-transiting exoplanet. This can result in a large uncertainty in the value of P_n inferred from the amplitude of the phase curve (Burrows et al. 2008). However, the large phase offset observed in υ And b implies a large P_n despite the large amplitude of the phase variation.

The thermal phase curve of HD 189733 b has been observed using Spitzer at 3.6μm and 4.5μm (Knutson et al. 2012), at 8μm (Knutson et al. 2007) and at 24μm (Knutson et al. 2009). There are also multiple observations of the transits and eclipses at 8μm for this system (Agol et al. 2010). The combined analysis of these results by Knutson et al. (2012) shows that heat recirculation from the day-side to the night-side is efficient for this relatively cool hot Jupiter ($T_{\text{day}} \approx 1200$ K) and that this recirculation leads to a peak in the thermal phase effect that occurs ~ 25 degrees before opposition.

Cowan et al. (2012) obtained Warm Spitzer photometry covering the complete 26 hour orbit of the very hot Jupiter WASP-12 b at $3.6\,\mu$m and $4.5\,\mu$m. They found that their interpretation of the lightcurves depends on the assumptions made about the nature of the systematic noise in the lightcurves and that red noise is the dominant source of uncertainty in their analysis. Nevertheless, they were able to show that the thermal phase variation in WASP-12 b is large, indicative of poor day-to-night heat redistribution ($P_n \lesssim 0.1$). The small offset they observe between the phase of maximum brightness and secondary eclipse (16 ± 4 degrees) in the $4.5\,\mu$m data is consistent with this interpretation. The phase offset at $3.6\,\mu$m could not be determined unambiguously from their data.

Although thermal phase curves are only currently available for a few systems, there does appear to be a pattern of weak recirculation for the hottest planets. Cowan & Agol (2011) have looked for trends in the value of $T_{\text{day}}/T_{\text{sub}}$, where T_{sub} is the equilibrium temperature of the sub-stellar point, in a sample of 24 transiting exoplanets with secondary eclipse measurements. This quantity will depend on both the albedo of the planet and the recirculation efficiency, but a large value can only be obtain if both the albedo and the recirculation efficiency are low. Cowan & Agol found that this is the case for all of the 6 hottest planets ($T_{\text{day}} \geqslant 2400$ K) in their sample and point out that this is, in general terms, the expected behviour given that the radiative timescale scales as T^{-3} whereas the advective timescale (which they assume to be of-order the local sound speed) scales as $T^{-0.5}$. This simple scaling argument does not explain the apparent transition in behaviour at $T_{\text{day}} \approx 2400$ K but Perna et al. (2012) do observe a transition at about this temperature in their suite of three-dimensional circulation models for hot Jupiters. This is mainly due to the change in the ratio of the radiative and advective timescales, with the presence of an atmospheric inversion playing a lesser role in determining the recirculation efficiency. This transition may also be related to the onset of ionisation of alkali metals in the planet's atmosphere, leading to severe magnetic drag (Perna et al. 2010). There is an ongoing debate as to whether the resulting Ohmic dissipation can transport energy into the interior of the planet and so explain the very large radii observed for

---

[1] The brightness temperatures are not necessarily equal since the SED from the day-side and night-side may be different.

some hot Jupiters (Laughlin et al. 2011; Rauscher & Menou 2012; Perna et al. 2012; Huang & Cumming 2012).

Here we present Warm Spitzer photometry covering the complete orbit of the very hot Jupiter WASP-18 b. This exoplanet is unusual for its combination of short orbital period (0.945 d) and high mass ($10\,M_{\rm Jup}$), which results in strong tidal interactions between the planet and the star (Hellier et al. 2009). Southworth et al. (2009) derived accurate masses and radii for the star and planet in the WASP-18 system based on high quality optical photometry of the transit and the spectroscopic orbit from Hellier et al.. Nymeyer et al. (2011) used Spitzer photometry in all four IRAC bands covering the secondary eclipse of WASP-18 to measure the brightness temperature of the day side from $3.6\,\mu$m to $8.0\,\mu$m. The high brightness temperatures derived ($\sim 3200\,$K) imply that WASP-18 b has near-zero albedo and almost no redistribution of energy from the day side to the night side of the planet.

Our primary aim is to use our Warm Spitzer photometry at $3.6\,\mu$m and $4.5\,\mu$m to measure the amplitude, phase and shape of the thermal phase effect. We also use these data to re-measure the secondary eclipse depths at $3.6\,\mu$m and $4.5\,\mu$m for comparison with the results of Nymeyer et al. (2011). We measure the times of eclipse and transit from our data and from new optical photometry of several transits and use these together with published times of mid-eclipse to re-measure the eclipse ephemeris and to look for possible variations in the period. We consider the likelihood that WASP-18 has a stellar companion based on published radial velocity data and new high-resolution imaging at H-band and K-band. The contamination of the lightcurve for a hot Jupiter system by a companion star has the potential to bias the results obtained if not properly accounted for. Companions stars may also play a role in the formation and evolution of some hot Jupiter systems (Fabrycky & Tremaine 2007; Mardling 2007). Our analysis also provides an accurate characterisation of the primary eclipse (transit) which can be used in combination with other data to re-measure the mass and radius of the star and planet.

2 OBSERVATIONS

2.1 Spitzer photometry

We were awarded *Spitzer* General Observer time during Cycle 6[2] to observe two complete orbits of WASP-18 with IRAC (Fazio et al. 1998), one orbit with each of the two IRAC channels operating during the warm mission. Observations with channel 1 (3.6μm) were obtained on 2010 January 23, observations with channel 2 (4.5μm) were obtained on 2010 August 23. On both dates, 243 200 images with an exposure time of 0.36s were obtained in sub-array mode. The total duration of each sequence of observations is 29 hours. In addition, a sequence of 64 sub-array images also with an exposure time of 0.36s were obtained immediately after the observations of WASP-18 at a slightly offset position. These were used to check for hot pixels or other image artifacts on

the detector. We used Basic Calibrated Data (BCD) processed with version S18.18 of the Spitzer IRAC pipeline for our analysis.

2.2 AO imaging

We obtained adaptive optics high resolution H- and K-band images of WASP-18 using the NICI instrument at Gemini South. The observations were obtained on the night of 2010 December 27 under good seeing ($0.5 - 0.6\,$arcsec). The instrument was configured with the CLEAR focal plane mask and the H 50/50 beam-splitter, and we used the narrow band filters $K_{\rm cont}$ ($2.2718\,\mu$m) and FeII ($1.644\,\mu$m) in the red and blue channels, respectively. We observed the target at five dither positions corresponding to the center and corners of a square of side 6 arcsec. At each dither position we obtained three images consisting of the co-addition of 3 exposures of 1.5 s. The full-width at half-maximum (FWHM) of the point spread function (PSF) in these images was 0.065 arcsec in the FeII filter and 0.073 arcsec in the $K_{\rm cont}$ filter.

Data reduction consisted of subtracting a sky image, dividing by the flat field, and fixing bad pixels by interpolating from neighbouring pixels. The sky image was created from the median combination of the images at the different dither positions after masking out the star signal in each image. The reduced images were registered to a common position and field orientation and then combined using the median value of each pixel. No other point source was detected in the resulting images. The sensitivity of our AO imaging to detect faint companions was determined by first computing the median absolute deviation of the pixel values within annuli of various radii and width equal to one PSF FWHM. The resulting contrast curve was then properly scaled, and verified to be adequate, by adding and recovering (by visual inspection) fake companions in the images at various separation and with various contrasts. In doing this last exercise we used both the K- and H-band images to differentiate speckles from true companions, which display a different chromatic behaviour. Using this approach, we estimate the detection limits in difference of magnitudes to be 4.0 mag at $\geqslant 0.2''$, 5.4 mag at $\geqslant 0.4''$ and 6.0 mag at $\geqslant 0.5''$. Finally, we note the presence of a faint ghost in the image at 13 pixel ($0.23''$) separation and contrast of $\sim$4.1 mag in the $K_{\rm cont}$ filter and $\sim$5.9 mag in the FeII filter.

2.3 TRAPPIST photometry

Five transits of WASP-18 b were observed with the 60 cm robotic telescope TRAPPIST[3] (Jehin et al. 2011; Gillon et al. 2012) located at ESO La Silla Observatory (Chile). TRAPPIST is equipped with a thermo-electrically-cooled $2k \times 2k$ CCD camera with a field of view of $22' \times 22'$ (pixel scale = 0.65 arcsec pixel^{-1}). The first four transits were observed in an Astrodon '$I + z$' filter that has a transmittance > 90 per cent from 750 nm to beyond 1100 nm, the red end of the effective bandpass being defined by the spectral response of the CCD. The last transit was observed in the Sloan z' filter. For all transits, the telescope was slightly defocused to minimize pixel-to-pixel effects and to optimize

Table 1. Details of the transit lightcurves obtained with TRAPPIST for WASP-18. For each lightcurve we list the observation date, the filter used, the number of measurements, and the exposure time.

Date	Filter	N_p	T_{exp} [s]
2010 Sep 30	$I+z$	712	12
2010 Oct 02	$I+z$	977	8
2010 Dec 23	$I+z$	688	6
2011 Jan 08	$I+z$	648	6
2011 Nov 10	z'	624	10

the observational efficiency. For each run, the stellar images were kept on the same pixels, thanks to 'software guiding' system deriving regularly astrometric solutions on the science images and sending pointing corrections to the mount if needed. Table 1 gives the logs of these TRAPPIST observations.

After a standard pre-reduction (bias, dark, flatfield correction), the stellar fluxes were extracted from the images using the IRAF/DAOPHOT[4] aperture photometry software (Stetson 1987). For each transit, several sets of reduction parameters were tested, and we kept the one giving the most precise photometry for the stars of similar brightness as WASP-18. After a careful selection of reference stars, differential photometry was obtained.

3   SPITZER DATA ANALYSIS

3.1   Conversion to flux and noise model

We converted the BCD images from units of MJy/steradian to mJy using the values for the pixel size at the centre of the subarray provided in the image headers ($1.225'' \times 1.236''$ for channel 1, $1.205'' \times 1.228''$ for channel 2). We used the raw images together with the values of the gain and readout noise for each channel to calculate the noise level in each pixel assuming Poisson counting statistics.

3.2   Image times

BCD data in sub-array mode are delivered as FITS files containing a data cube of 64 images of 32×32 pixels per file. We used the FITS header keyword BMJD_OBS to assign a Barycentric UTC modified Julian date (BMJD) to the start of the exposure for the first image in the data cube. The BMJD of the mid-exposure time for each image in the data cube was then calculated using the values for the start and end times of the integration from the FITS header (AINT-BEG and ATIMEEND) to calculate the time taken to obtain the 64 images and assuming that these images were uniformly spaced in time.

Long observing sequences such as the ones we have used

---

[4] IRAF is distributed by the National Optical Astronomy Observatory, which is operated by the Association of Universities for Research in Astronomy, Inc., under cooperative agreement with the National Science Foundation.

for WASP-18 cannot be executed using standard observing modes so multiple instrument engineering requests (IERs) are used to obtain the data. The images obtained in the second of the two IERs used for our WASP-18 observations do not have the coordinates of the target in the FITS header and so the light-time correction to the solar system barycentre are incorrect for these images. We calculated the light-time correction for the images obtained before the interruption from the difference in the keyword values BMJD_OBS − MJD_OBS. We then use a linear extrapolation of this light-time correction as a function of MJD_OBS to calculate the BMJD of the images obtained after the interruption based on their MJD_OBS values. The uncertainty in the exposure time introduced by this procedure is negligible.

3.3   Outlier rejection

We compared each image to the other 63 images in the same data cube in order to identify discrepant data points in the images. We are particularly concerned here with identifying discrepant pixel values that may affect the photometry of the target. As the target moves during the sequence of 64 images, we use a robust linear fit (least absolute deviation) to the 64 pixel values from each file for each pixel to predict the expected value for each pixel value in each image. We then flag the pixels in each image that deviate from their expected value by more than 5 times their standard error. We find that the number of pixels flagged using this method is much larger than expected given the known incidence of cosmic ray hits on the IRAC detectors. This discrepancy is due to a few pixels well away from the target position that are noisier than predicted by our noise model. As these pixels have no effect on our photometry and a negligible effect on the estimate of the background level we ignore this discrepancy. We also flagged any pixels in our images that are flagged as bad pixels in the "Imask" file provided for each BCD file by the Spitzer IRAC pipeline.

3.4   Sky background estimate

We use the mean of the image pixel values excluding those within 10 pixels of the target position to estimate the background value in each image. Values more than 4 standard deviations from the mean and flagged pixels were ignored in the calculation. We used a Gaussian fit to a histogram of these pixel values to estimate the standard deviation of the background pixel values, σ_{bg}. The number of points used to estimate the background was ≈ 700. Typical values of σ_{bg} are 0.0033 mJy/pixel for channel 1 and 0.0025 mJy/pixel for channel 2.

3.5   Aperture photometry

We tried three different methods to measure the location of the star on the detector, the DAOPHOT CNTRD and GCNTRD algorithms and a least-squares fit of a bivariate Gaussian distribution to an 11×11 sub-image centred on the nominal star position. We refer to this latter algorithm as the GAUSS2D method. We used a fixed value for the full-width at half-maximum of FWHM= 1.25 pixels for both axes of
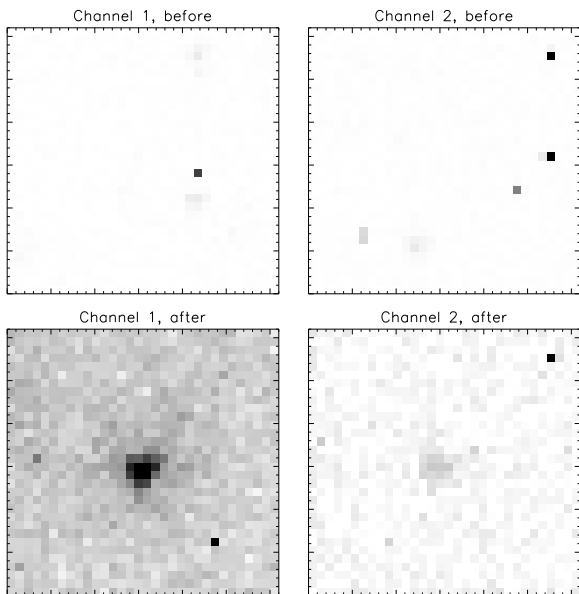
Figure 1. Images obtained before and after our WASP-18 observations. All images are linearly scaled (inverse grey scale) between 0 and 10 MJy/sr. The "before" images are 30 s exposures in the region of IC 2560. The "after" images are the median of the 64 offset sky images with an exposure time of 30 s each.

the Gaussian profile in the GAUSS2D method based on the results of fitting the images with the FWHM as a free parameter. The CNTRD algorithm determines the position where the derivatives of the image values go to zero. The GCNTRD algorithm fits a Gaussian profile to the marginal x and y distributions of the image values. We set the input parameters to CNTRD and GCNTRD to run on a sub-image of 5×5 pixels around the target position. We compare the performance of these different algorithms below.

We used the IDL Astronomy Users library[5] implementation of the DAOPHOT APER procedure (Stetson 1987) to perform synthetic aperture photometry on our images. We used the 2006 November version of this procedure which allowed us to use the option to use an exact calculation of the intersection between a circular aperture and square pixel for correct weighting of pixels at the edge of the aperture. We used 13 aperture radii uniformly distributed from 1.5 pixels to 4.5 pixels. The results we obtained for larger aperture radii were not useful because the lightcurves have much lower signal-to-noise due to the additional background noise. Fluxes measured from images containing any flagged pixels in the aperture were rejected from further analysis, although much less than 1 per cent of images were affected in this way. The median number of rejected pixels per image is 2.

3.6 Image persistence

Our IRAC images are affected by image persistence, particularly the channel 1 images. This can be seen in the offset sky images obtained immediately after our WASP-18 observations (Fig. 1). The resulting image artifacts are more

diffuse than the stellar images and look more like the logarithm of the point spread function, as described in the IRAC instrument handbook (Version 2.0.1, p. 116) . The image artifact in the channel 1 offset sky images has up to about 0.6 mJy per pixel in the channel 1 image and a total of about 6 mJy within an aperture with a radius of 5 pixels. For comparison, a typical channel 1 image of WASP-18 has a peak flux of $50-70$ mJy/pixel and a total flux of 163 ± 3 mJy within an aperture of the same radius, so the image artifact affects the photometry of WASP-18 by a few per cent. For the channel 2 data the corresponding figures are a total of about 1 mJy/pixel in the artifact compared to 42 mJy/pixel in the peak and a total flux of 103 ± 1 mJy in the images of WASP-18 so for this channel image persistence affects the photometry by about 1 per cent.

The IRAC instrument handbook describes the behaviour of image persistence artifacts in the IRAC arrays during the warm mission. In channel 1 the artifacts decay exponentially with a timescale of about 4.5 hours. Channel 2 residuals start out as positive, but then become negative with a decay timescale of a few minutes.

For channel 1 data we make the assumption that the image artifact will be approximately constant after some time during the exposure sequence comparable to the decay timescale. To correct for the effect of image persistence we create a "master offset image" from the median of the 64 offset sky images, subtract the background value from this image and then subtract the result from the images of WASP-18. This correction will be inaccurate for some fraction of the data at the start of the observing sequence while the image persistence builds-up. We discuss this point further below.

For the channel 2 data it is not clear how the image artifact affects the photometry of WASP-18. The interval between the end of the observing sequence for WASP-18 and the start of the offset sky image is 49 s, which is comparable to the decay timescale for the artifact. The exact form and timescale for the decay of the artifact is not known so it is not even possible to make a precise estimate of contribution of the image artifact to the measured flux for WASP-18. However, it is likely that the image artifact contributes less than 2 per cent given the decay timescale for this feature is a few minutes. We did attempt to measure the decay timescale from the data taken subsequent to our own observations, but the artifact was not detectable in those images. For the channel 2 data we treat the contribution of the image persistence artifact as an additional source of uncertainty in our analysis.

3.7 Initial assessment of the data

The flux of WASP-18 measured with an aperture radius of 4.5 pixels is shown for both channels in Fig. 2. Also shown in this figure are the positions of the star on the array calculated using the GAUSS2D method. The coordinates x and y are measured relative to the centre of a corner pixel in the sub-array. The form of the variations in the x,y positions measured using the GCNTRD and CNTRD algorithms are similar, but the amplitudes of the variations are less and there is an offset between these values and the results of the GAUSS2D method. For example, the y positions measured for the channel 1 data using the GCNTRD method have me-

dian value of 14.95 with 98 per cent of the data in the range $y = 14.78 - 14.95$, cf. a median value of 14.88 and range $y = 14.65 - 14.99$ for the GAUSS2D method.

The feature that stands out from Fig. 2 is the well-known correlation between the measured flux and the position of the star on the detector, particularly in channel 1. This position-dependent sensitivity variation (PDSV) makes it difficult to see the transit and secondary eclipse in these "raw" aperture flux measurements. The channel 2 data appear to be less affected by PDSV, so the transit and secondary eclipse can be seen in the raw flux measurements. PDSV is a combination of the "pixel phase effect" described in the IRAC instrument handbook (Version 2.0.1, p. 45) and pixelation noise. The pixel phase effect is a variation in the sensitivity of each detector pixel that depends on the distance of the stellar image from the centre of the pixel. The motion in the x and y directions for our channel 2 data result in a smaller variation in the distance of the star from the centre of the pixel compared to the channel 1 data, which may partly explain why the data quality is better in this channel (Anderson et al. 2011). Pixelation noise affects synthetic aperture photometry with small aperture radii because for a pixel at the edge of the aperture, the fraction of the flux falling within that pixel is not the same as the fraction of the aperture within the pixel.

3.8 Analysis of the thermal phase effect

3.8.1 Correction for PDSV

The usual method developed to correct for PDSV in IRAC data for observations of the secondary eclipses of hot Jupiters is to include parameters in the least-squares fit of an eclipse model to the data to represent the PDSV. This is usually a simple linear or quadratic relation between sensitivity and each of the coordinates x and y (e.g., Beerer et al. 2011; Anderson et al. 2011). Ballard et al. (2010) have developed an alternative method to correct for PDSV in their Warm Spitzer $4.5\mu m$ observations of GJ 436. They created a *pixel sensitivity map* from the data themselves. This approach was straightforward in the case of GJ 436 because the lightcurve of the target is expected to be constant apart from the possible presence of transits affecting a small fraction of the data. The pixel sensitivity map generated by Ballard et al. for the IRAC channel 2 shows complex structure that they describe as "corrugation ... low-level sinusoidal-like variations with a separation of approximately 5/100ths of a pixel between peaks". A similar concept based on bi-linear interpolation rather than a smoothed look-up table has been developed by Stevenson et al. (2012) and applied to Spitzer photometry of HD 149026 b.

For our WASP-18 data we are interested in characterising the amplitude and shape of the phase variation as well as measuring the shape and depths of the transit and secondary eclipse. The phase variation has a period comparable to the length of the observing sequence so it is important to understand any correlations between the correction for the PDSV and the parameters of the lightcurve model. The phase variation of WASP-18 can be modelled approximately as a sinusoidal variation in flux with P=0.94 d. For example, in the worst case scenario, if the position of the target on the detector also varied approximately sinusoidally with

approximately the same period, then it would become impossible to determine whether any variation in the measured flux with $P \approx 0.94$ is due to the flux variation of WASP-18 or due to the PDSV.

Understanding the correlations between the lightcurve model parameters and the correction for PDSV is problematic in the case of our WASP-18 data because of the large number of parameters required to model the complete lightcurve plus the large number of parameters that may be required to characterise the complex structure ("corrugation") in the PDSV. One method we experimented with was to use the pixel sensitivity map method of Ballard et al. (2010) applied to the residuals to a least-squares fit of a lightcurve model. This approach can be applied iteratively until the solution and pixel sensitivity map converge. The problem with this approach is that it becomes difficult to identify correlations between the lightcurve model parameters and the pixel sensitivity map. We avoided this problem by excluding the data during the transit and occultation from our analysis of the thermal phase effect. The main advantage of this approach is that fitting a model to the data between the eclipses can be reduced to a linear least-squares problem. This makes is straightforward to find the best solution of the problem and to investigate the correlations between the free parameters of the model.

3.8.2 Model for PDSV and the thermal phase effect

Our model for the measured magnitude of the system between the eclipse and transit is

$$
\begin{aligned}
m_i = {} & c_{0,0} + \sum_{j=1}^{N_{\cos}} a_j \cos(j\phi_i) + \sum_{k=1}^{N_{\sin}} b_k \sin(k\phi_i) \\
& + \sum_{\iota=1}^{N_x} c_{\iota,0} p_\iota(x_i') + \sum_{\kappa=1}^{N_y} c_{0,\kappa} p_\kappa(y_i') \\
& + \sum_{\lambda=1}^{N_{xy}} \sum_{\mu=1}^{N_{xy}} c_{\lambda,\mu} p_\lambda(x_i') p_\mu(y_i'),
\end{aligned}
\tag{1}
$$

where m_i is the magnitude of WASP-18 at time t_i; $\phi_i = 2\pi(t_i - T_0)/P$ is the orbital phase relative to the time of mid-transit, T_0; p_n is a Legendre polynomial of order n; $x_i' = (x_i - \bar{x})/(x_{\max} - x_{\min})$ and similarly for y_i' ($x_{\min}$ is the minimum value of x_i, etc.). We use the values $T_0 =$ BMJD 54220.98163 for the time of mid-transit and $P = 0.94145299$ d for the orbital period from Hellier et al. (2009) throughout this paper unless otherwise stated. By using Legendre polynomials and normalized coordinates (x_i', y_i') we find that we can use singular value decomposition to find solutions of this least-squares problem for Legendre polynomials up to at least 12th order. This is sufficient to model the corrugations with a scale of 0.05 pixels seen by Ballard et al. if they are present in our data.

3.8.3 Linear decorrelation against position

In Fig. 3 we show the result of using the simplest reasonable model for our data, in which the magnitude of the phase variation varies sinusoidally and the PDSV is linear in x and y, i.e.,

$$ m_i = c_{0,0} + a_1 \cos(\phi_i) + b_1 \sin(\phi_i) + c_{1,0} p_1(x_i') + c_{0,1} p_1(y_i'). $$

Note that our calculations are done using magnitudes, but we plot the results as fluxes and quote parameter values in unit of per cent. The least-squares fit of this model to
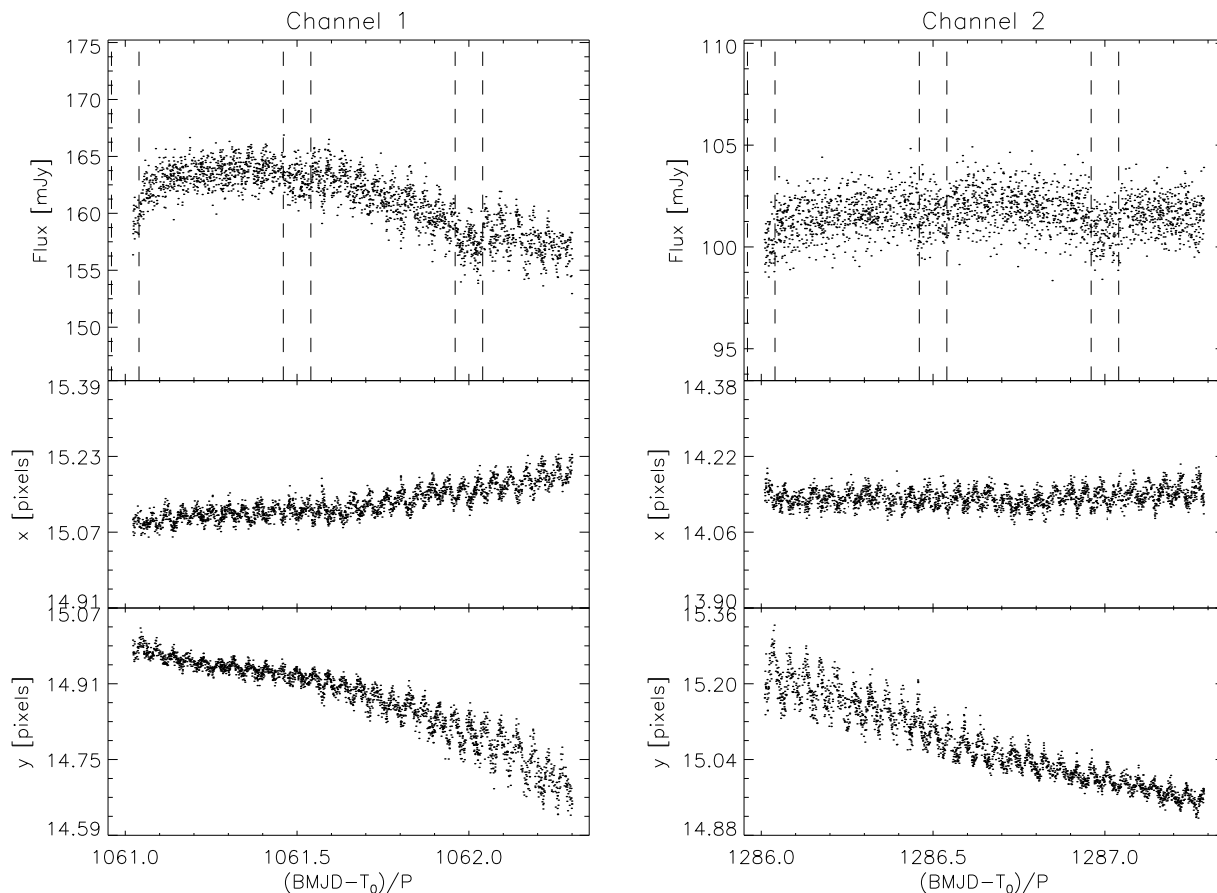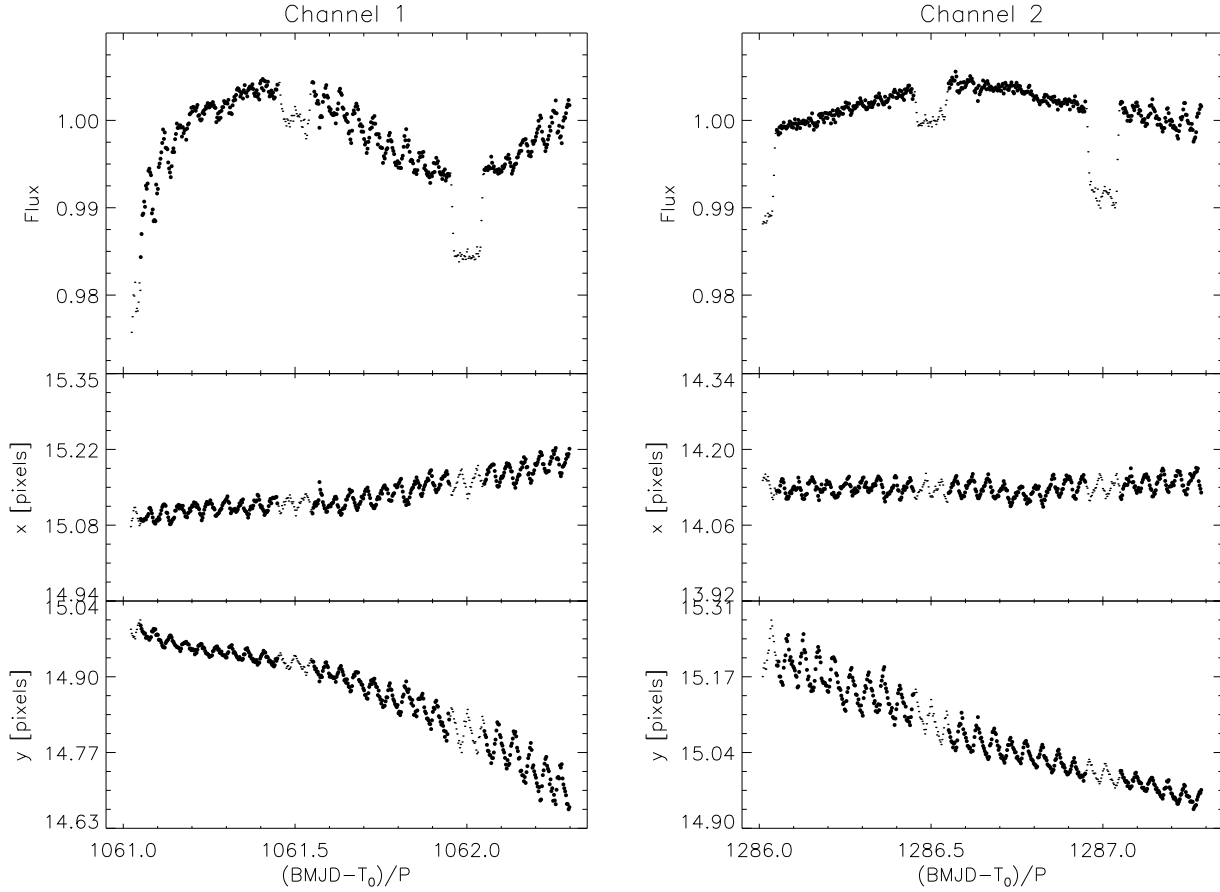
Figure 2. The flux of WASP-18 measured in IRAC channel 1 (left panel) and channel 2 (right panel) measured with a circular aperture of radius of 4.5 pixels.. The position of the star on the array measured using the GAUSS2D method is shown below each panel. For clarity, we have only plotted a random selection of 1 per cent of the data here. Dashed lines indicate the start and end times of the transit and secondary eclipse assuming a duration of 0.08 d for each and assuming that the secondary eclipse occurs at phase 0.5.

the unbinned aperture photometry outside of eclipse and transit is used to determine the coefficients of the model for the PDSV. We then apply this correction to all the data. The results in Fig. 3 are for an aperture radius of 2.5 pixels for both apertures and target positions measured using the GAUSS2D method. This is the combination of aperture radius and positions that gave the lowest RMS residual for the data between the transit and eclipse. Results for other apertures and for CNTRD and GCNTRD methods are similar. It is clear that a linear correction is insufficient to fully remove the effect of the PDSV, but this simple model does show clearly some features of our data. Firstly, we see that the eclipse and transit are clearly visible in both channels. Two transits are visible in the channel 2 data but the first transit is not seen clearly in the channel 1 data because there is a large "ramp" affecting the first few hours of the data. There is a cosine-like variation in flux observed in both channels with the maximum flux occurring near phase 0.5 (secondary eclipse). Part of this signal is the phase variation we wish to measure. However, there must also be some instrumental component or other systematic effect that contributes to this variation because the phase variation due to the planet cannot have an amplitude larger than the secondary eclipse depth.

The obvious suspect for the systematic noise source in the channel 1 data is the image artifact shown in Fig. 1. The "ramp" is the right size (≈ 3 per cent) and builds up over the same sort of timescale as the known decay timescale of this artifact. Our interpretation of this lightcurve is that the image artifact builds up over the first $6-8$ hours before reaching an approximate equilibrium between the arrival of new photons from WASP-18 and its own decay timescale.

We have tried several methods to account for this ramp-like feature in the data but none of these methods is any better than the more pragmatic approach of simply excluding the first $6-8$ hours of the channel 1 data. Without going into the details of these various methods, we can state here that we almost always found that the amplitude of the phase variation measures in channel 1 was similar to the depth of the secondary eclipse and often was slightly larger. It is possible to create models for the systematic noise in the channel 1 lightcurves that achieve more physically realistic (lower) values for the amplitude of the phase variation, but these models are not based on any physical model of the instrumental noise, i.e., they are arbitrary, and they require several additional free parameters that are often not well constrained by the data or any physical understanding of what these parameters represent. The overall quality

Figure 3. The flux of WASP-18 measured in IRAC channel 1 (left panel) and channel 2 (right panel) after a linear correction for position dependent sensitivity variations and a simple sinusoidal model for the phase variation. The zero-point of the flux scale is set from the mean flux during secondary eclipse. Observations obtained during the transit and secondary eclipse (small points) were excluded from the calculation of the coefficients for the decorrelation. The data have been binned into 0.0025 d bins for display purposes only.

of the decorrelated lightcurve obtained with these arbitrary and complex models of the the instrumental noise is also not much better than the best results presented below for the partial lightcurve. Clearly, a more complete understanding of the instrumental noise in IRAC for warm mission observations would be a great help for the interpretation of our data, but in the absence of this we present the results for the partial lightcurve and make an attempt to quantify the extent to which instrumental noise introduces systematic errors in our results.

3.8.4   *Optimum decorrelation against position.*

We used the model given in equation (1) to fit the data for channel 1 and channel 2 excluding data within 0.05 d of mid-transit and mid-eclipse and also excluding the first 60 000 observations (7.3 hours of data) for channel 1. We used $N_{\cos} = 2$ and $N_{\sin} = 1$ to model the phase variation of WASP-18. The sine term allows for a phase shift from phase 0.5 for the time of maximum brightness and the first harmonic of the cosine variations (coefficient a_2) allows for some optimisation of the shape of this phase variation. To model the PDSV we tried $N_x = N_{xy} = N_y/2 = 1, 2, \ldots 6$. We use $N_y = 2N_x$ because there is a larger range of motion

in the y direction. We fit these models to the lightcurves for all combinations of aperture size and position measurement methods. We used the Bayesian information criterion (BIC) to identify the combination of (N_x, N_y, N_{xy}) that provides the best compromise between quality of fit and number of free parameters for a given lightcurve. We calculated the BIC using the expression

$$\mathrm{BIC} = \chi^2 + N_{\mathrm{par}} \log_e(N),$$

where N_{par} is the number of free parameters and N is the number of observations. We used the RMS of the residuals to identify the aperture size and position measurement method that give the best lightcurves. For both channels we find the best results are obtained for $(N_x, N_y, N_{xy}) = (5, 10, 5)$ with positions measured using the CNTRD method and an aperture radius of 2.25 pixels. These models and lightcurves are shown in Fig. 4 and the parameters of interest are given in Table 2. The standard error estimates given in Table 2 account for the correlations between parameters (Press et al. 1992) although the correlation coefficients between the parameters in this table and all other parameters in the model are small (< 0.3).

In Fig. 5 we show how the parameters a_1, a_2 and b_1 obtained for $(N_x, N_y, N_{xy}) = (5, 10, 5)$ vary as a function of

Table 2. Results of linear least squares fits to the phase variation between eclipses using the model given in equation (1). These results are for $(N_x, N_y, N_{xy}) = (5, 10, 5)$ with positions measured using the CNTRD method and an aperture radius of 2.25 pixels. N is the number of points included in the fit and BIC is the Bayesian information criterion as defined in the text. A is the amplitude of the thermal phase effect and $\phi_{\max}$ is the phase of maximum brightness relative to phase 0.5. Random and systematic errors are given for each quantity in that order.

Parameter	Channel 1	Channel 2
a_1 [%]	$0.148 \pm 0.005 \pm 0.01$	$0.183 \pm 0.004 \pm 0.01$
a_2 [%]	$0.003 \pm 0.005 \pm 0.01$	$0.023 \pm 0.005 \pm 0.01$
b_1 [%]	$0.001 \pm 0.003 \pm 0.01$	$-0.006 \pm 0.003 \pm 0.01$
A [%]	$0.296 \pm 0.009 \pm 0.02$	$0.366 \pm 0.007 \pm 0.02$
$\phi_{\max}$	$0.001 \pm 0.003 \pm 0.01$	$-0.010 \pm 0.006 \pm 0.02$
N	133124	179851
χ^2	142398.6	216717.3
BIC	142928.2	217259.0
RMS [%]	0.539	0.717

aperture radius and position measurement method for our various lightcurves. Also plotted in Fig. 5 are the amplitude of the phase variation and the offset from phase 0.5 to the time of maximum brightness in phase units. There is some dependence on aperture radius for these results, e.g., the value of a_1 for both channels show a trend towards smaller values with increasing radius. We also see that there is worse agreement between the results for different position measurement methods for smaller apertures as a result of the increased sensitivity of the pixelation noise to small differences in the assumed position. For all of the coefficients in both channels we see that the results vary by about ± 0.01 per cent as a function of aperture radius. We therefore assume that systematic noise limits the accuracy of these results to ± 0.01 per cent.

Despite the limit of ± 0.01 per cent in the accuracy of these results, we are able to draw some definite conclusions about the thermal phase effect in WASP-18. Firstly, the amplitude of the thermal phase effect is very similar to the depth of the secondary eclipse. This can be seen in Fig. 4 and by comparing the values for the amplitude in Table 2 to the eclipse depths given in Table 3. Secondly, the offset between phase 0.5 and the time of maximum brightness due to the thermal phase effect is consistent with 0 to within about 0.01 phase units for the channel 1 data and 0.02 phase units for the channel 2 data. Thirdly, the parameter a_2 is also consistent with the value 0 so the shape of the thermal phase variation is sinusoidal to within the limits sets by the systematic noise.

3.9 Eclipse model

We tried several different methods to model the entire lightcurve for each channel including both eclipses, the phase variation and PDSV, but were not able to find any method that gave reliable results. We suspect that there is some factor other than position on the detector that introduces systematic noise at the level of ~ 0.01 per cent with a timescale of $\sim$day. This can be seen in Fig. 4, where there are clear

systematic errors remaining in the lightcurve at this level. These systematic errors are not removed by increasing the complexity of the model used for the PDSV. It will be difficult to identify this additional factor given that little information about the shape of the point spread function can be measured from the undersampled IRAC images.

There are many published studies that have used IRAC photometry obtained over ~ 5 hours of observation to successfully model hot Jupiter eclipses, so we decided to only model the data within 0.1 phase units of the primary and secondary eclipses. We fit these data simultaneously using a single model to account for the true flux variations of the system. We then account for systematic errors in the measured flux independently for the data around each eclipse.

We have used the NDE lightcurve model (Nelson & Davis 1972; Popper & Etzel 1981; Etzel 1981) to model the primary and secondary eclipses in our lightcurves. This model uses biaxial ellipsoids to approximate to projected area of the star/planet. Giménez (2006) has shown that this model used with an integration ring size of one degree (as we have done) can be used to model planetary transits with a precision of $\sim 4 \times 10^{-5}$, which is sufficient for our purposes. From inspection of our model lightcurves we find that $\sim \frac{1}{4}$ of the model data points during primary eclipse are affected by numerical noise at this level and that there is no numerical noise during secondary eclipse. We created a double-precision version of the NDE model that has negligible numerical noise, but that runs appreciably slower than the original single-precision code. We used our double-precision version to verify that the numerical noise in the single-precision version has a negligible effect on our results, so all the results presented here are based on the single-precision version.

We use the NDE model to calculate $\ell_s(\phi)$ and $\ell_p(\phi)$, the contribution of the star and planet, respectively, to the total apparent flux at any given phase, ϕ, including the effects of tidal distortion and eclipses. Note that ℓ_s and ℓ_p include the effects of the eclipses and transits and the ellipsoidal variation of both star and planet. To model the variation in magnitude due to the phase effect of the planet we use the harmonic series

$$h(\phi) = a_1 \cos(\phi) + b_1 \sin(\phi) + a_2 \cos(2\phi) - h_{\max},$$

where the values of a_1, b_1 and a_2 are taken from the least-squares fit to the data between transit and eclipse for the same aperture size and position measurement method and $h_{\max}$ is chosen such that the maximum value (corresponding to minimum flux) of $h(\phi)$ is 0.

The apparent magnitude of the system is then given by

$$m_i = m_0 - 2.5 \log\left[\ell_s(\phi_i) + \ell_p(\phi_i)\right] + \ell_p(\phi_i)h(\phi_i)/\ell_{p,\max},$$

where $\ell_{p,\max}$ is a normalization factor. Our calculations are done using magnitudes but we present the results in flux units or as percentages.

In addition, we model the PDSV independently for the data around primary and secondary eclipse using Legendre polynomial functions of the x and y position plus an optional linear function of time. For each set of lightcurve model parameters we calculate the optimum values of the PDSV model parameters using singular value decomposition to fit the residuals from the lightcurve model.

The parameters of the NDE lightcurve model of rele-
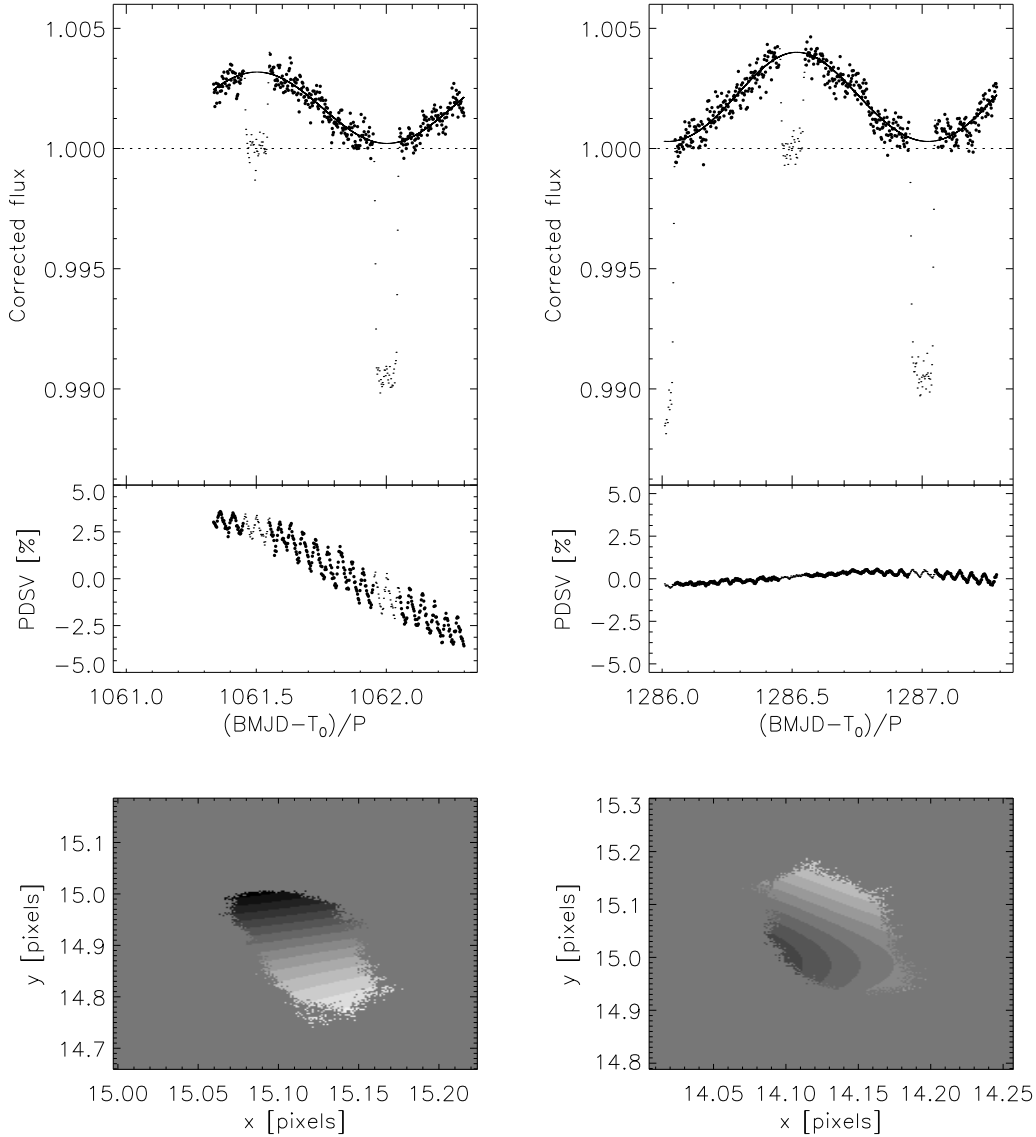
Figure 4. The flux of WASP-18 measured in IRAC channel 1 (left panel) and channel 2 (right panel) in an aperture of radius 2.25 pixels after correction for position dependent sensitivity variations (PDSV) for the parameter sets $(N_{\cos}, N_{\sin}, N_x, N_y, N_{xy}) = (2, 1, 5, 10, 5)$ and positions measured with the CNTRD method. Data are plotted averaged in 200 s bins for clarity and the best-fit sinusoidal model is also shown. The mean value in secondary eclipse is indicated with a dotted line. Note that data in eclipse (small points) are not included in the fit. The PDSV model is shown as a function of time in the middle panels and as a function of position as a grey-scale plot in the lower panels. The grey-scale is linear between ± 4 per cent for channel 1 and 1 per cent for channel 2 with positive values being white.

vance to our study are: J, the surface brightness of the planet in units of the central surface brightness of the star excluding the thermal phase contribution; $r_1 = R_{\rm star}/a$, the radius of the star in units of the semi-major axis; $r_2 = R_{\rm planet}/a$, the radius of the planet in units of the semi-major axis; i, the inclination, $u_\star$, the linear limb-darkening coefficient for the star; $e\cos(\omega)$ and $e\sin(\omega)$, where e is the orbital eccentricity and ω is the longitude of periastron. We fix the mass ratio of the system at the value $m_{\rm planet}/m_{\rm star} = 0.01$. We did not use this combination of parameters directly as free parameters in our least-squares fitting because there are significant correlations between them. Instead, we introduce
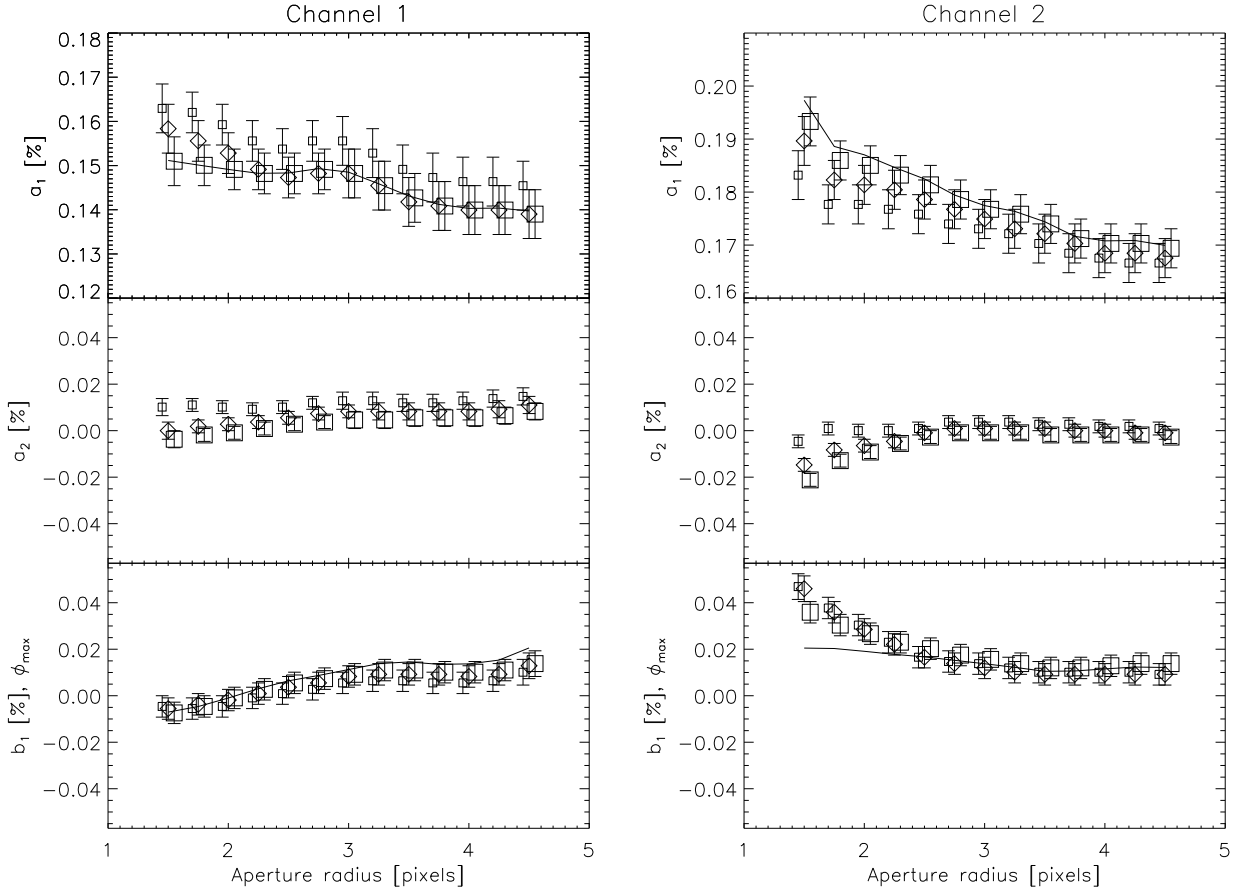
the following parameters which are more directly related to the observed features of the lightcurve: $\Delta m_{\rm tr}$, $\Delta m_{\rm oc}$, W, S. The parameters of the NDE lightcurve model are then calculated as follows:

$$k = \frac{r_2}{r_1} = \sqrt{\frac{\ln(10)}{2.5}\Delta m_{\rm tr}};$$

$$r_1 = \frac{\pi}{2\sqrt{k}}\sqrt{W^2(1 - S^2)};$$

$$r_2 = kr_1;$$

$$b = \sqrt{\frac{(1 - k)^2 - S^2(1 + k)^2}{1 - S^2}};$$

Figure 5. Coefficients of the sinusoidal model for the phase variation in WASP-18 as a function of aperture radius. The parameter set $(N_x, N_y, N_{xy}) = (5, 10, 5)$ was used for the correction for position dependent sensitivity. Plotting symbols are as follows: CNTRD – squares; GCNTRD – diamonds; GAUSS2D – filled circles. The solid line in the upper panels shows the semi-amplitude of the phase variation for the CNTRD results. The solid line in the lower panel is the the phase offset from phase 0.5 for time of maximum brightness for the thermal phase effect derived from the CNTRD results. Points have been offset horizontally by ±0.05 for clarity.

$$i = \cos^{-1}(br_1);$$

$$J = \frac{1 - u_\star/3}{k^2\left(\frac{2.5}{\ln(10)\Delta m_{oc}} - 1\right)}.$$

These parameters are adapted from Seager & Mallén-Ornelas (2003) so that, for a circular orbit, Δm_{tr} is the depth of the primary eclipse in magnitudes, Δm_{oc} is magnitude difference between the flux duration occultation and the minimum of the thermal phase curve; W is the width of the transit in phase units and S is the duration of the ingress phase of the transit in units of W. The intermediate variables used here are k, the radius ratio and b, the impact parameter. We also include a correction to the time of mid-transit compared to the ephemeris of Hellier et al., ΔT_0.

We are careful here to define what we mean by the depth of the secondary eclipse because the variation in flux due to the thermal phase effect on the timescale of the eclipse is comparable to the precision with which we can measure the depth from our photometry (~ 0.01 per cent) and the maximum of the thermal phase effect may not occur at mid-eclipse. For ease of calculation, interpretation and com-

parison with other measurements, we simply measure the mean flux during occultation (excluding ingress and egress phases), f_{in}, and the mean flux either side of the eclipse in a region ± 0.1 phase units around the time of mid-eclipse, f_{out} and define the secondary eclipse depth to be $D = \frac{f_{out} - f_{in}}{f_{out}}$. The fluxes are measured from the lightcurve corrected for PDSV.

There are some second-order effects not accounted for by our model. We do not account for the brightness distribution on the day-side of the planet, but this will have a negligible effect on our results given that the thermal phase effect is not strongly peaked and is symmetrical about phase 0.5, so this distribution will be approximately uniform and symmetrical. Doppler boosting is negligible compared to our signal-to-noise ($\lesssim 0.001$ per cent). We make a small correction to the results for the effects of image persistence in the channel 2 data by assuming a dilution of the eclipses for 1±1 per cent. We have applied a correction to the apparent times of secondary eclipse for the light travel time across the orbit of $2a/c \approx 20\,$s so that the times and phases quoted here are the true time of mid-occultation relative to the apparent time of mid-transit. We also apply a correction to the values of $e\cos(\omega)$ quoted below for this light travel time.
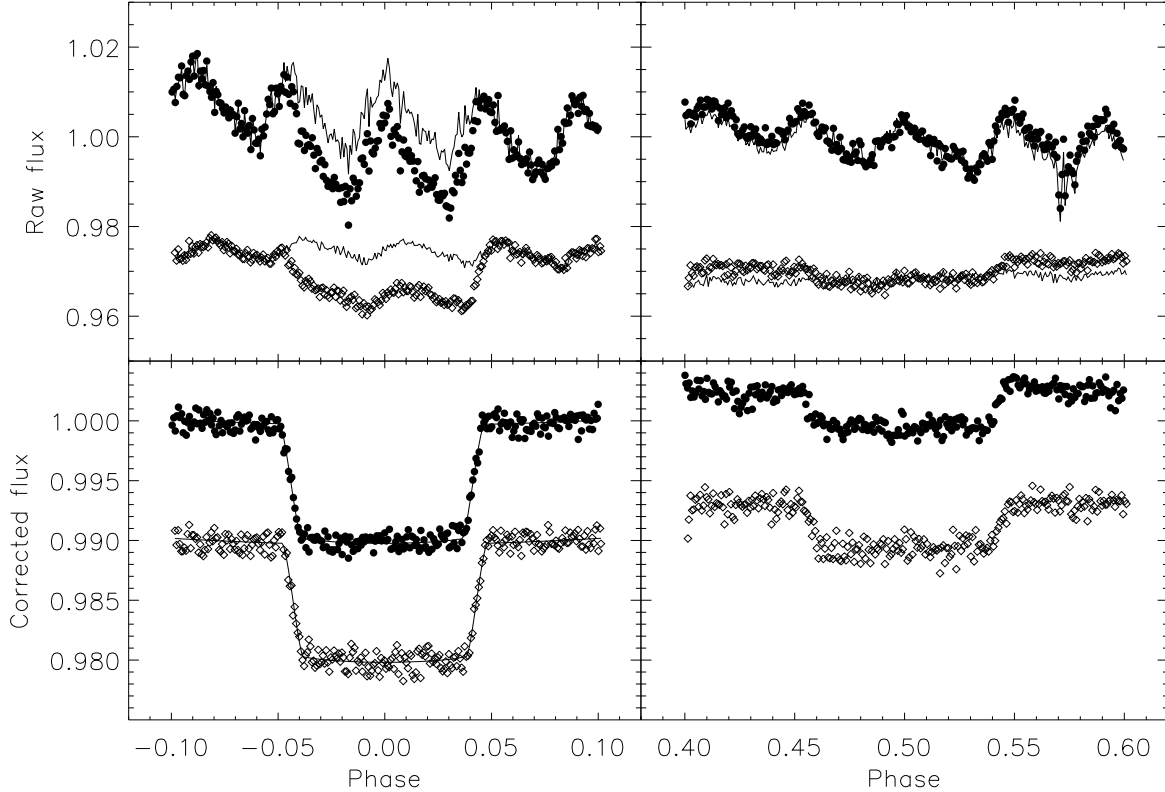
Figure 6. Upper panel: Raw photometry for an aperture radius of 3 pixels (filled symbols – channel 1, open symbols – channel 2) together with the correction for PDSV based on positions measured using the CNTRD method (lines). Lower panel: Photometry corrected for PDSV (points) and models fit by least-squares (lines). The channel 2 data have been vertically offset by 0.03 in the upper panel and 0.01 in the lower panel. In both panels the data and models are plotted in 60 s bins.

We use the simplex algorithm of Nelder & Mead (1965) to optimise the least-squares fit of our model to the lightcurves. The simplex algorithm is a simple way to optimize a least-squares solution given an initial set of parameters, but it is not guaranteed to find the global minimum value of χ^2 in the parameter space. In this case we are able to estimate accurate initial values for the most important parameters and so any solution will not be very far from the global minimum. However, we do find that numerical noise prevents us from using this algorithm by itself to find the optimum solution. We work around this problem by testing many initial starting values. We found that the solution with the lowest value of χ^2 sometimes has parameters that are slightly biased when compared to other solutions with similar values of χ^2 as a result of the numerical noise. We avoid this problem by taking the median value of each parameter for all solutions with χ^2 within 5 of the minimum as our best estimate of the parameter.

The results for the depths of the eclipses and the RMS of the residuals for each data set are shown in Fig. 7. The depth of the primary eclipse (transit) can vary slightly with wavelength because the apparent radius of the planet will be larger at wavelengths where the atmosphere has a large opacity (Seager & Sasselov 2000). The size of this effect is approximately $2HR_{\mathrm{planet}}/R_{\mathrm{star}}^2$ where H is the atmospheric scale height. In practice, for WASP-18 b the size of this ef-

fect is negligible (≈ 0.001 per cent) because the large surface gravity of this massive planet makes the scale height of the atmosphere ($\sim 40\,\mathrm{km}$) much smaller than the size of the star. It can be seen from Fig. 7 that the solutions with the lowest RMS occur for an aperture radius 2 pixels, but the transit depths for channel 1 and 2 disagree by about 0.01 per cent for these data sets.

The transit depths measured in channels 1 and 2 are consistent with each other for an aperture radius of 3 pixels and lie near the centre of the range of values obtained. The best fit to the lightcurves for an aperture radius of 3 pixels using the positions from the GCNTRD method are shown in Fig. 6 and the parameters for the model used are given in Table 3. It can be seen that there is some residual correlated noise in the lightcurves after removal of the model for the PDSV. We quantified this residual correlated noise by calculating the RMS of the residuals after binning for a range of bin sizes (Pont et al. 2006). The results are shown in Fig. 8 and compared to the expectation for pure photon noise. At the timescale of the eclipse it can be seen that the channel 2 data are only weakly affected by correlated noise ($\lesssim 0.005$ per cent) but the channel 1 data are affected correlated noise at a level of $0.005 - 0.01$ per cent, particularly for the data covering occultation.

Given that there is significant correlated noise in our data, we decided to calculate the random error on our model
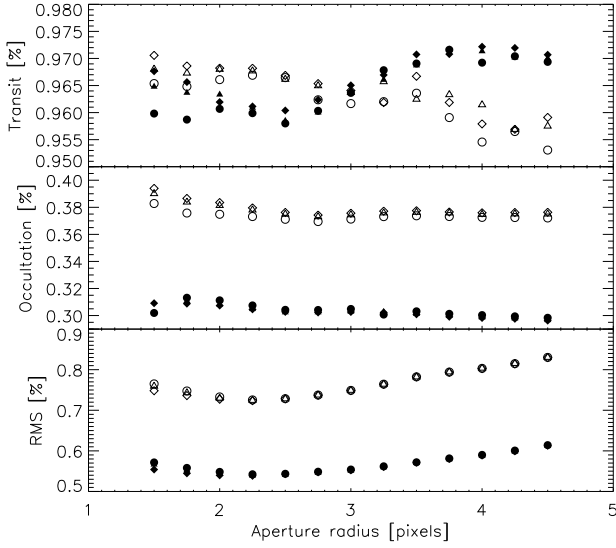
Figure 7. Depths of eclipses for transit and occultation measured by fitting the eclipses. Channel 1 data are shown with filled symbols, channel 2 data with open symbols. Different symbols denote different position measurement methods. The RMS of the residuals of the fits are also shown using the same symbols.

parameters using the "prayer-bead" method (Pont et al. 2006). This uses a circular permutation of the residuals by a random number of steps to create mock data sets. We applied the circular permutation to the residuals of the primary and secondary eclipses independently and then used the simplex algorithm to fit models to 1024 mock data sets. The standard deviation of parameters from the fits is used to calculate the random errors for the model parameters given in Table 3 based on the analysis of the lightcurves for an aperture radius of 3 pixels using the positions from the GCNTRD method. The random errors quoted include the effect of the uncertainty in correcting for image persistence in the data. We use the range of values from the different apertures and position measurement methods to estimate the systematic errors on each parameter. The distribution of the parameters for the mock data sets is shown for some parameters of interest in Fig. 9. As can be seen from this figure, the eclipse depths derived from the mock data sets can be biased by up to ∼ 0.005 per cent from the actual value. This is an consequence of the correlated noise in the residuals. We also used the results from these mock data sets to calculate the Pearson correlation coefficient, r, for all pairs of free parameters used in the least-squares fit. There is a weak anti-correlation between W and S ($r \approx -0.5$), and a weak correlation between W and $e \sin(\omega)$ ($r \approx 0.5$), but the other free parameters are uncorrelated, as expected.

4 OPTICAL VARIABILITY

The interpretation of our data would be considerably complicated by any intrinsic variability of the star WASP-18.

We have analysed the WASP lightcurves of WASP-18 to determine whether they show periodic modulation due to the combination of magnetic activity and the rotation
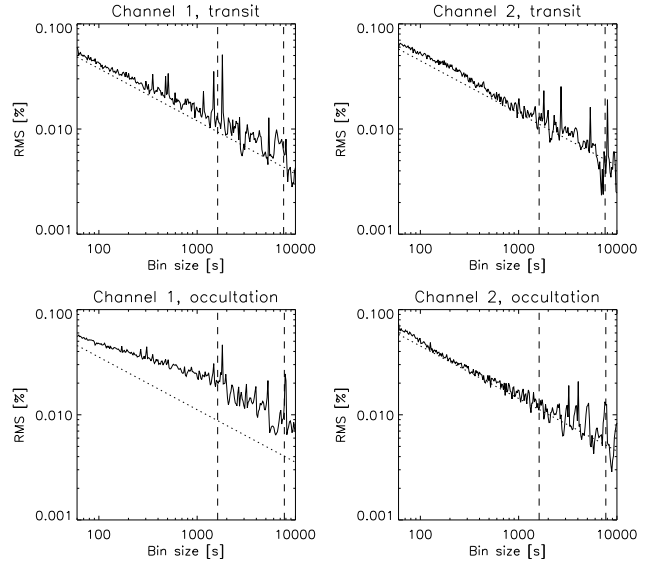
Figure 8. RMS of the residuals after binning as a function of bin size (solid line) compared to the predicted photon noise (dotted line). The vertical, dashed lined in each panel shows the duration of eclipse and the duration of ingress/egress.
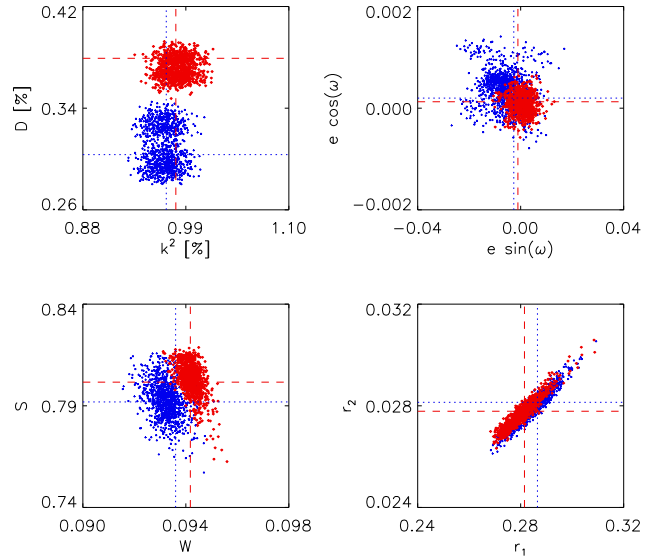
Figure 9. Parameter correlation plots from our residual permutation error analysis for channel 1 (blue crosses) and channel 2 (red diamonds). Our adopted values for each channel are indicated using dotted and dashed lines for channel 1 and 2, respectively.

of the star. The observed value of $V_{\rm rot} \sin I = 11 \, {\rm km \, s^{-1}}$ (Hellier et al. 2009) together with the stellar radius imply a rotation period of about 6 d for WASP-18. We used the sine-wave fitting method described in Maxted et al. (2011) to calculate periodograms over 4096 uniformly spaced frequencies from 0 to 1.5 cycles/day. The false alarm probability (FAP) for the strongest peak in these periodograms was calculated using a boot-strap Monte Carlo method also described in Maxted et al. (2011). Variability due to star spots is not expected to be coherent on long timescales as a consequence

Table 3. Results of least squares fits to the primary and secondary eclipses. $J' = J/(1 - u_\star/3)$ is the ratio of the integrated surface brightness of the star and the day-side of the planet. Other symbols are defined in the text. Random and systematic errors are given for each parameter in that order. Parameters that can be derived from the analysis of the optical TRAPPIST lightcurves are also given in the final column.

Parameter	Channel 1	Channel 2	TRAPPIST
$\Delta m_{\rm tr}$ [%]	$0.969 \pm 0.013 \pm 0.007$	$0.979 \pm 0.013 \pm 0.009$	0.965 ± 0.056
$\Delta m_{\rm oc}$ [%]	$0.015 \pm 0.014 \pm 0.009$	$0.028 \pm 0.006 \pm 0.017$	
D [%]	$0.304 \pm 0.017 \pm 0.009$	$0.379 \pm 0.008 \pm 0.013$	
W	$0.0936 \pm 0.0005 \pm 0.0003$	$0.0942 \pm 0.0003 \pm 0.0002$	0.0946 ± 0.0011
S	$0.792 \pm 0.009 \pm 0.0007$	$0.802 \pm 0.008 \pm 0.007$	
$u_\star$	$0.06 \pm 0.03 \pm 0.06$	$0.07 \pm 0.03 \pm 0.04$	
$e \cos(\omega)$	$0.0002 \pm 0.0004 \pm 0.0003$	$0.0001 \pm 0.0002 \pm 0.0003$	
$e \sin(\omega)$	$-0.003 \pm 0.006 \pm 0.004$	$-0.001 \pm 0.003 \pm 0.002$	
ΔT_0 [s]	$-109 \pm 8 \pm 0$	$-108 \pm 8 \pm 0$	
r_1	$0.287 \pm 0.006 \pm 0.004$	$0.282 \pm 0.005 \pm 0.004$	0.291 ± 0.017
r_2	$0.0281 \pm 0.0006 \pm 0.0003$	$0.0278 \pm 0.0005 \pm 0.0005$	0.0286 ± 0.0026
k	$0.0982 \pm 0.0007 \pm 0.0004$	$0.0987 \pm 0.0006 \pm 0.0004$	0.0983 ± 0.0030
b	$0.39 \pm 0.06 \pm 0.04$	$0.32 \pm 0.06 \pm 0.04$	0.41 ± 0.15
i	$83.6 \pm 1.0 \pm 0.7$	$84.8 \pm 1.1 \pm 0.8$	83 ± 3
J'	$0.33 \pm 0.02 \pm 0.02$	$0.40 \pm 0.01 \pm 0.02$	
Phase of mid-occultation	$0.5003 \pm 0.0006 \pm 0.0004$	$0.5002 \pm 0.0003 \pm 0.0005$	
$N_{\rm transit}$	33996	35261	3649
$N_{\rm occultation}$	36847	34355	
χ^2	74213.9	90739.5	2768.5
RMS [%]	0.55	0.75	0.40

of the finite lifetime of star-spots and differential rotation in the photosphere and so we analysed the data from each observing season independently. We removed the transit signal from the data prior to calculating the periodograms by subtracting a simple transit model from the lightcurve. In addition to the 2 seasons of data from Hellier et al. (2009) we also analyse 6041 observations obtained during the 2012 Jun – Dec observing season. This date range covers the time of our Spitzer channel 2 observations.

We did not find any significant periodic signals (FAP< 0.05) for WASP-18 apart from frequencies near 1 cycle/day due to instrumental effects. We examined the distribution of amplitudes for the most significant frequency in each Monte Carlo trial and used these results to estimate a 95 per cent upper confidence limit of 0.1 per cent for the amplitude of any periodic signal in these WASP lightcurves. Beaulieu et al. (2010) have shown that the amplitude of the modulation at IRAC wavelengths due to star spots in solar-type stars is an order-of-magnitude smaller than at optical wavelengths. We conclude that any intrinsic variability of WASP-18 due to star spots has a negligible impact on our analysis.

5 ECLIPSE EPHEMERIS

The analysis above provided two new, precise measurements of the time of mid-occultation and mid-transit. In addition we have 5 new times of mid-transit from our TRAPPIST observations. A global analysis of the five lightcurves was performed with the MCMC software described by Gillon et al. (2012). In addition to the baseline model and to the transit ephemeris and shape parameters, the timings of the transits were included as free parameters, the transit ephemeris

being constrained by normal priors based on the ephemeris presented by Nymeyer et al. (2011). The details of this analysis are similar to the ones described in Gillon et al. (2012). The parameters derived from the least-squares fit to the 5 lightcurves are shown in Table 3. It can be seen that there is very good agreement between the parameters of the system derived from the optical and infrared lightcurves.

We have also measured a new time of mid-transit by using a least-squares fit of the NDE lightcurve model to the 2010 season of WASP data. The time of mid-transit quoted is close to the mid-point of dates of observation for these data and the standard error on the time of minimum is calculated using the prayer-bead method. All these times of mid-eclipse are given in Table 4 together with other published times of mid-eclipse.

We used a least squares fit with a single value of the period and the times of mid-transit and mid-occultation as free parameters to determine a following linear ephemeris.

$$\text{TDB(mid - transit)} = 2455265.5525(1) + 0.9414523(3) \cdot E$$

$$\text{TDB(mid - occult.)} = 2455266.0234(3) + 0.9414523(3) \cdot E$$

The χ^2 value for this fit was 21.8 with 11 degrees-of-freedom so the standard errors quoted in the final digits here have been scaled by $\sqrt{21.8/11}$. We also tried a quadratic ephemeris fit to the same data but found that this did not significantly improve the fit. The residuals from this $O - C$ diagram for this linear ephemeris is shown in Fig. 10. It can be seen that the times of eclipse for WASP-18 have not varied by more than about 100 s over 3 years.

Table 4. Apparent Barycentric Dynamical Time (TDB) of mid-transits (tr) and mid-occultation (oc) for WASP-18. The cycle number is calculated from our updated linear ephemeris and $O-C$ is the residual from this ephemeris. Times of mid-occultation have been corrected for light-travel time across the orbit.

BJD$_{TDB}$ − 2450000		Type	Cycle	O − C	Source
4664.9061	±0.0002	tr	−576	0.00013	1
4820.7168	±0.0007	oc	−411	0.00019	2
4824.4815	±0.0006	oc	−407	−0.00097	2
5220.8337	±0.0006	oc	14	−0.00006	a
5221.3042	±0.0001	tr	15	0.00017	a
5392.6474	±0.0004	tr	197	0.00014	3
5419.0083	±0.0012	tr	225	0.00015	b
5431.7191	±0.0003	oc	238	−0.00114	a
5432.1897	±0.0001	tr	239	−0.00087	a
5470.7885	±0.0004	tr	280	−0.00057	c
5473.6144	±0.0009	tr	283	0.00098	c
5554.5786	±0.0005	tr	369	0.00026	c
5570.5842	±0.0006	tr	386	0.00118	c
5876.5559	±0.0013	tr	711	0.00097	c

1: Triaud et al. (2010); 2: Nymeyer et al. (2011); 3: *http://var.astro.cz/ETD/*; a: Spitzer IRAC; b: WASP; c: TRAPPIST.
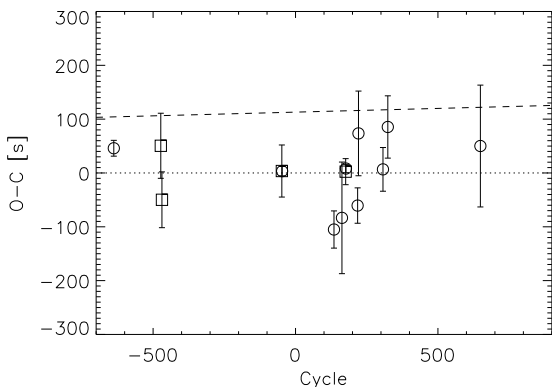
Figure 10. Residuals from our best-fit linear ephemeris for observed times of mid-transit (circles) and mid-occultation (squares) for WASP-18. The difference between our ephemeris and the ephemeris of Hellier et al. is also shown (dashed line).

6 WASP-18 STELLAR PARAMETERS

A total of 21 individual HARPS spectra of WASP-18 were co-added to produce a single spectrum with a typical S/N of around 200:1. The analysis was performed using the methods given in Doyle et al. (2012). The H_α and H_β lines were used to give an initial estimate of the effective temperature (T_{eff}). The surface gravity ($\log g$) was determined from the Ca I lines at 6162Å and 6439Å (Bruntt et al. 2010), along with the Na I D lines. Additional T_{eff} and $\log g$ diagnostics were performed using the Fe lines. An ionisation balance between Fe I and Fe II was required, along with a null dependence of the abundance on either equivalent width or excitation potential (Bruntt et al. 2008). This null dependence was also required to determine the micro-turbulence (ξ_t). The parameters obtained from the analysis are listed

Table 5. Stellar parameters of WASP-18 from our spectroscopic analysis.

Parameter		Value
T_{eff}	[K]	6400 ± 75
$\log g$		4.29 ± 0.10
ξ_t	[km s^{-1}]	1.20 ± 0.08
$v \sin i$	[km s^{-1}]	12.1 ± 0.5
[Fe/H][a]		0.10 ± 0.08
Mass[b]	[$M_\odot$]	1.26 ± 0.09
Radius[b]	[$R_\odot$]	1.25 ± 0.15
Sp. Type[c]		F6
Distance	[pc]	130 ± 20

[a][Fe/H] is relative to the solar value obtained by Asplund et al. (2009). [b] Mass and radius estimated using the Torres et al. (2010) calibration. [c] Spectral Type estimated from T_{eff} using the table in Gray (2008).

in Table 5. The value of [Fe/H] was determined from equivalent width measurements of several unblended lines, and additional least squares fitting of lines was performed when required. The quoted error estimates include that given by the uncertainties in T_{eff}, $\log g$, and ξ_t, as well as the scatter due to measurement and atomic data uncertainties.

The projected stellar rotation velocity ($v \sin i$) was determined by fitting the profiles of several unblended Fe I lines. A value for macroturbulence (v_{mac}) of 4.6 ± 0.3 km s^{-1} was assumed, based on the calibration by Bruntt et al. (2010). An instrumental FWHM of 0.07 ± 0.01 Å was determined from the telluric lines around 6300Å. A best fitting value of $v \sin i = 10.9 \pm 0.7$ km s^{-1} was obtained.

The rotation rate ($P = 5.8 \pm 0.8$ d) implied by the $v \sin i$ gives a gyrochronological age of $\sim 1.1^{+4.7}_{0.6}$ Gyr using the Barnes (2007) relation. The value of T_{eff} derived from our spectroscopic analysis agrees well with the value 6455 ± 70 K derived by Maxted et al. (2011) from optical and near-infrared photometry using the infrared flux method. The distance derived here assuming that WASP-18 is a main-sequence star and quoted in Table 5 is consistent with the value 100 ± 10 pc derived from the Hipparcos parallax (van Leeuwen 2007).

7 PHYSICAL PARAMETERS

Our new photometric and spectroscopic results allow for an improved determination of the physical properties of the WASP-18 system. We performed this analysis following the method of Southworth (2009), which requires as its input parameters measured from the lightcurves and spectra, plus tabulated predictions of theoretical models. From the lightcurves we adopted $r_1 = 0.284 \pm 0.005$, $r_2 = 0.0280 \pm 0.0005$ and $i = 84° \pm 1°$. The stellar T_{eff} and [Fe/H] were taken from the spectroscopic determination in the previous section, and the star's velocity amplitude was taken to be $K_1 = 1816.7 \pm 1.9$ m s^{-1} (Triaud et al. 2010).

An initial value of the velocity amplitude of the planet, K_2, was used to calculate the physical properties of the system with the physical constants listed by Southworth (2011). The mass and [Fe/H] value of the star were then used to obtain the expected T_{eff} and radius, by interpolation within

Table 6. Derived physical properties of the WASP-18 system. Parameter values are shown with random and, where appropriate, systematic errors, respectively.

Parameter	Value
M_A ($M_\odot$)	$1.295 \pm 0.052 \pm 0.027$
R_A ($R_\odot$)	$1.255 \pm 0.027 \pm 0.009$
$\log g_A$ (cgs)	$4.353 \pm 0.017 \pm 0.003$
ρ_A ($\rho_\odot$)	0.655 ± 0.035
M_b (M_{Jup})	$10.52 \pm 0.28 \pm 0.15$
R_b (R_{Jup})	$1.204 \pm 0.027 \pm 0.008$
g_b (m s^{-2})	179.9 ± 6.4
ρ_b (ρ_{Jup})	$5.64 \pm 0.31 \pm 0.04$
T_{eq} (K)	2411 ± 35
a (AU)	$0.02055 \pm 0.00028 \pm 0.00014$
Age (Gyr)	$0.4^{+0.8}_{-0.9}{}^{+0.5}_{-0.3}$

one set of tabulated predictions from stellar theory. K_2 was refined in order to find the best agreement between the observed and expected T_{eff}, and the measured r_1 and expected $\frac{R_1}{a}$. This was performed for ages ranging from the zero-age main sequence to when the star was significantly evolved ($\log g < 3.5$), in steps of 0.01 Gyr. The overall best fit was found, yielding estimates of the system parameters and also the stellar age.

This procedure was performed separately using five different sets of stellar theoretical models (see Southworth 2010, for details) plus a calibration of stellar properties based on well-studied eclipsing binary star systems (Enoch et al. 2010), with calibration coefficients from Southworth (2011). The results are given in Table 6, where we quote the mean value for each parameter, the random error and an estimate of the systematic error from the range of values derived from the different stellar models, where appropriate. It can be seen from Table 6 that the results from different models are consistent to within the random errors on each parameter.

In comparison to previous work, we have derived more precise radii, surface gravities and densities, for both components. We constrain the age of the star to be less than 1.7 Gyr, consistent with the gyrochronological age derived above.

8 POSSIBILITY OF CONTAMINATION BY A COMPANION STAR

We have estimated the probability that our Spitzer photometry of WASP-18 is contaminated by the "third-light" from a companion star. It is not possible to detect a modest amount of third-light contamination directly from the lightcurve itself because its only effect is to reduce the depths of the eclipses. It would be possible to find a good fit to a lightcurve affected by third-light contamination, but the parameters of the lightcurve model would be biased, e.g., k would be too small.

Our calculation is based on the upper limit from our AO observations of 4.0 magnitudes for the brightness of any companion between $0.2 - 2$ arcseconds from WASP-18 and the upper limit of 43 m s^{-1} y^{-1} over a baseline of 500 days to the variation in the mean radial velocity of WASP-18

from Triaud et al. (2010). We assume that the probability distribution for the mass, eccentricity and period of the hypothesised companion is the same as the distributions for companions to solar-type stars from Raghavan et al. (2010). We approximated the distribution of companion masses using a uniform distribution from $0.2 M_\odot$ to $0.8 M_\odot$ and used a uniform eccentricity distribution from 0 to 1. We then created a set of 65536 simulated binary stars with randomly selected periods, masses and eccentricities according to these distributions and randomly orientated orbits. We found that of these simulated binary stars, approximately 55 per cent would have been resolved by our AO imaging at the distance of WASP-18; 20 per cent would have orbital periods less than 500 days and a semi-amplitude of 43 m s^{-1} or more and 25 per cent would show a change in radial velocity of 43 m s^{-1} or more over 500 days. This leaves only 5 per cent of hypothesised binaries as not detectable given our AO imaging and the published radial velocity data. The probability that WASP-18 has a stellar companion is further reduced because the overall binary fraction observed for planet hosting stars is approximately 25 per cent (Raghavan et al. 2010). An M-dwarf at the same distance as WASP-18 just below out detection limit of 4.0 magnitudes in the K-band at 0.2 arcsec would contribute no more than 5 per cent of the light at 4.5μm. The more stringent limit of 6.0 magnitudes in the K-band that applies for separations of $0.5 - 2.0$ arcsec corresponds to an M-dwarf that contributes no more than 1 per cent at 4.5μm. Of the simulated binary stars approximately 45 per cent would be detected at this resolution.

In conclusion, our AO imaging and the published radial velocity data show that it is unlikely that WASP-18 has a stellar companion that significantly contaminates our Spitzer photometry.

9 DISCUSSION

The values of D in Table 3 are in very good agreement the values 0.31 ± 0.02 at 3.6μm and 0.38 ± 0.02 per cent at 4.5μm measured independently by Nymeyer et al. (2011). Their analysis of the secondary eclipse depths in 4 IRAC passbands suggests that the day-side atmosphere of WASP-18 is likely to feature a temperature inversion. For zero albedo and zero redistribution of heat to the night side of the planet the integrated brightness temperature for the day-side is $T_{\varepsilon=0} = \left(\frac{2}{3}\right)^{1/4} T_0 = 3110 \pm 35$ K (Cowan & Agol 2011). For black-body emission this implies eclipse depths of 0.329 ± 0.005 at 3.6μm and 0.379 ± 0.011 per cent at 4.5μm, both in good agreement with the observed values. Zero-redistribution of heat within the atmosphere is also consistent with our observation that the peak of the thermal phase curve occurs close to the time of mid-occultation. Little can be said about the chemical composition of the day-side atmosphere at this stage because no strong molecular absorption or emission features have been detected from these secondary eclipse depth measurements.

The amplitude of the thermal phase curve we have measured and the lack of a significant offset between the maximum in this curve and the time of mid-eclipse are both consistent with the conclusion based on the secondary eclipse depths that the albedo and recirculation efficiency for WASP-18 are both very low. This is consistent with

the hypothesis that very hot Jupiters have weak recirculation based mainly on secondary eclipse depth measurements alone (Cowan & Agol 2011). The good agreement between the recirculation efficiency inferred from the eclipse depths and measured from the thermal phase curve for WASP-18 strengthens this conclusion.

The stellar limb darkening at infrared wavelengths is lower than at optical wavelengths and so the transit produces a more "box-shaped" eclipse. This, combined with the precise photometry that is possible with Spitzer IRAC data, results in more precise estimates for parameters such as R_{star}/a, R_{planet}/a and $k = R_{planet}/R_{star}$. Our results for these parameters agree well with the results of Southworth et al. (2009). The agreement with the results of Triaud et al. (2010) is less good mainly because they find a larger stellar radius than our study ($R_{star}/a = 0.313 \pm 0.010$). The values of $e\cos(\omega)$ and $e\sin(\omega)$ derived from our analysis agree well with those of Triaud et al., but the value of $e\sin(\omega) = 0.0085 \pm 0.0009$ they derive from their high quality radial velocity data is much more precise than ours and points to a small but significantly non-zero eccentricity. Arras et al. (2012) have argued that the small value of this apparent eccentricity combined with longitude of periastron very close to $\omega = 90°$ is exactly the signal expected due to surface flows induced by tides on the planet. Their conclusion that the orbital eccentricity of WASP-18 b is less than 0.009 is consistent with the results of our analysis, although we are not able to confirm whether $e \ll 0.009$ as they suggest.

The measurement of the thermal phase effect for hot Jupiters using a continuous set of observations over an orbital cycle with Warm Spitzer is not a well-established technique, so it is useful to compare our experience of observing WASP-18 with the results using a similar observing strategy for WASP-12 obtained by Cowan et al. (2012) and for HD 189733 by Knutson et al. (2012). We find that systematic errors of unknown origin limit the accuracy with which we can measure the amplitude of signals with time-scale comparable to the orbital period to about ± 0.01 per cent. The main difficulty that Cowan et al. report in their WASP-12 analysis is a signal on twice the orbital frequency in the $4.5\,\mu$m data that they tentatively attribute to the ellipsoidal modulation of WASP-12 b. However, as they make clear, this signal is not seen in their $3.6\,\mu$m data and may be due to "uncorrected systematic noise". The amplitude of this "$\cos(2\phi)$" signal in their $4.5\,\mu$m data is about ± 0.1 per cent, ten times larger than the level of systematic noise we find on these timescales. We do not see any signal for the $\cos(2\phi)$ harmonic in our $4.5\,\mu$m data greater than about 0.02 per cent. Knutson et al. use the wavelet-based method of Carter & Winn (2009) to account for systematic noise in their full-orbit lightcurves of HD 189733 by assuming that this noise has a power spectral density varying as 1/frequency. They find that the systematic noise contributes 0.0162 per cent of the total scatter in their channel 1 data – comparable to the level seen in our data – but only 0.0017 per cent in channel 2 – much less than we see in our data. A systematic application of the wavelet-based method to archival Spitzer data may be a useful way to better understand the systematic noise sources in this instrument and perhaps identify observing strategies that can reduce systematic noise levels.

10 CONCLUSIONS

The amplitude, shape and phase of the thermal phase effect we have measured from our Warm Spitzer lightcurves of WASP-18 are consistent with a sinusoidal variation with the same amplitude as and symmetric about the secondary eclipse, to within an accuracy ≈ 0.01 per cent set by some unknown source of systematic error. One contribution to this systematic error is likely to be the image persistence we observe from the offset images obtained immediately after our observations of WASP-18. This leads to the conclusion that WASP-18 b has a low albedo and that heat transport to the night-side of the planet is inefficient. This is the same conclusion reached by Nymeyer et al. (2011) based on the eclipse depths at $3.6\,\mu$m, $4.5\,\mu$m, $5.8\,\mu$m and $8.0\,\mu$m. The eclipse depths we measure at $3.6\,\mu$m and $4.5\,\mu$m are consistent with the previous measurements.

REFERENCES

Agol E., Cowan N. B., Knutson H. A., Deming D., Steffen J. H., Henry G. W., Charbonneau D., 2010, ApJ, 721, 1861

Anderson D. R., Smith A. M. S., Lanotte A. A., Barman T. S., Collier Cameron A., Campo C. J., Gillon M., Harrington J., Hellier C., Maxted P. F. L., Queloz D., Triaud A. H. M. J., Wheatley P. J., 2011, MNRAS, 416, 2108

Arras P., Burkart J., Quataert E., Weinberg N. N., 2012, MNRAS, 422, 1761

Asplund M., Grevesse N., Sauval A. J., Scott P., 2009, ARA&A, 47, 481

Ballard S., Charbonneau D., Deming D., Knutson H. A., Christiansen J. L., Holman M. J., Fabrycky D., Seager S., A'Hearn M. F., 2010, PASP, 122, 1341

Barnes S. A., 2007, ApJ, 669, 1167

Beaulieu J. P., Kipping D. M., Batista V., Tinetti G., Ribas I., Carey S., Noriega-Crespo J. A., Griffith C. A., Campanella G., Dong S., Tennyson J., Barber R. J., Deroo P., Fossey S. J., Liang D., Swain M. R., Yung Y., Allard N., 2010, MNRAS, 409, 963

Beerer I. M., Knutson H. A., Burrows A., Fortney J. J., Agol E., Charbonneau D., Cowan N. B., Deming D., Desert J., Langton J., Laughlin G., Lewis N. K., Showman A. P., 2011, ApJ, 727, 23

Bruntt H., Bedding T. R., Quirion P.-O., Lo Curto G., Carrier F., Smalley B., Dall T. H., Arentoft T., Bazot M., Butler R. P., 2010, MNRAS, 405, 1907

Bruntt H., De Cat P., Aerts C., 2008, A&A, 478, 487

Bruntt H., Deleuil M., Fridlund M., Alonso R., Bouchy F., Hatzes A., Mayor M., Moutou C., Queloz D., 2010, A&A, 519, A51

Burrows A., Budaj J., Hubeny I., 2008, ApJ, 678, 1436

Carter J. A., Winn J. N., 2009, ApJ, 704, 51

Charbonneau D., Allen L. E., Megeath S. T., Torres G., Alonso R., Brown T. M., Gilliland R. L., Latham D. W., Mandushev G., O'Donovan F. T., Sozzetti A., 2005, ApJ, 626, 523

Cooper C. S., Showman A. P., 2005, ApJ, 629, L45

Cowan N. B., Agol E., 2011, ApJ, 729, 54

Cowan N. B., Agol E., Charbonneau D., 2007, MNRAS, 379, 641

Cowan N. B., Machalek P., Croll B., Shekhtman L. M., Burrows A., Deming D., Greene T., Hora J. L., 2012, ApJ, 747, 82

Crossfield I. J. M., Hansen B. M. S., Harrington J., Cho J. Y.-K., Deming D., Menou K., Seager S., 2010, ApJ, 723, 1436

de Wit J., Gillon M., Demory B.-O., Seager S., 2012, arxiv:1202.3829

Deming D., Seager S., Richardson L. J., Harrington J., 2005, Nature, 434, 740

Doyle A. P., Smalley B., Maxted P. F. L., Anderson D. R., Collier-Cameron A., Gillon M., et al. 2012, MNRAS, submitted.

Enoch B., Collier Cameron A., Parley N. R., Hebb L., 2010, A&A, 516, A33+

Etzel P. B., 1981, in E. B. Carling & Z. Kopal ed., Photometric and Spectroscopic Binary Systems A Simple Synthesis Method for Solving the Elements of Well-Detached Eclipsing Systems. p. 111

Fabrycky D., Tremaine S., 2007, ApJ, 669, 1298

Fazio G. G., Hora J. L., Willner S. P., Stauffer J. R., Ashby M. L., Wang Z., Tollestrup E. V., Pipher J. L., Forrest W. J., McCreight C. R., Moseley S. H., Hoffmann W. F., Eisenhardt P., Wright E. L., 1998, in A. M. Fowler ed., Society of Photo-Optical Instrumentation Engineers (SPIE) Conference Series Vol. 3354 of Society of Photo-Optical Instrumentation Engineers (SPIE) Conference Series, Infrared array camera (IRAC) for the Space Infrared Telescope Facility (SIRTF). pp 1024–1031

Gillon M., Triaud A. H. M. J., Fortney J. J., Demory B.-O., Jehin E., Lendl M., Magain P., Kabath P., Queloz D., Alonso R., Anderson D. R., Collier Cameron A., Fumel A., Hebb L., Hellier C., Lanotte A., Maxted P. F. L., Mowlavi N., Smalley B., 2012, A&A, 542, A4

Giménez A., 2006, A&A, 450, 1231

Goodman J., 2009, ApJ, 693, 1645

Gray D. F., 2008, The Observation and Analysis of Stellar Photospheres. Cambridge University Press

Harrington J., Hansen B. M., Luszcz S. H., Seager S., Deming D., Menou K., Cho J. Y.-K., Richardson L. J., 2006, Science, 314, 623

Hellier C., Anderson D. R., Cameron A. C., Gillon M., Hebb L., Maxted P. F. L., et al. 2009, Nature, 460, 1098

Huang X., Cumming A., 2012, ApJ, 757, 47

Jehin E., Gillon M., Queloz D., Magain P., Manfroid J., Chantry V., Lendl M., Hutsemékers D., Udry S., 2011, The Messenger, 145, 2

Knutson H. A., Charbonneau D., Allen L. E., Fortney J. J., Agol E., Cowan N. B., Showman A. P., Cooper C. S., Megeath S. T., 2007, Nature, 447, 183

Knutson H. A., Charbonneau D., Cowan N. B., Fortney J. J., Showman A. P., Agol E., Henry G. W., Everett M. E., Allen L. E., 2009, ApJ, 690, 822

Knutson H. A., Howard A. W., Isaacson H., 2010, ApJ, 720, 1569

Knutson H. A., Lewis N., Fortney J. J., Burrows A., Showman A. P., Cowan N. B., Agol E., Aigrain S., Charbonneau D., Deming D., Désert J.-M., Henry G. W., Langton J., Laughlin G., 2012, ApJ, 754, 22

Laughlin G., Crismani M., Adams F. C., 2011, ApJ, 729, L7

Madhusudhan N., Harrington J., Stevenson K. B., Nymeyer S., Campo C. J., et al. 2011, Nature, 469, 64

Majeau C., Agol E., Cowan N. B., 2012, ApJ, 747, L20

Mardling R. A., 2007, MNRAS, 382, 1768

Maxted P. F. L., Anderson D. R., Collier Cameron A., Hellier C., Queloz D., Smalley B., Street R. A., Triaud A. H. M. J., West R. G., Gillon M., Lister T. A., Pepe F., Pollacco D., Ségransan D., Smith A. M. S., Udry S., 2011, PASP, 123, 547

Maxted P. F. L., Koen C., Smalley B., 2011, MNRAS, 418, 1039

Nelder J. A., Mead R., 1965, The Computer Journal, 7, 308

Nelson B., Davis W. D., 1972, ApJ, 174, 617

Nymeyer S., Harrington J., Hardy R. A., Stevenson K. B., Campo C. J., et al. 2011, ApJ, 742, 35

Perna R., Heng K., Pont F., 2012, ApJ, 751, 59

Perna R., Menou K., Rauscher E., 2010, ApJ, 724, 313

Pont F., Zucker S., Queloz D., 2006, MNRAS, 373, 231

Popper D. M., Etzel P. B., 1981, AJ, 86, 102

Press W. H., Teukolsky S. A., Vetterling W. T., Flannery B. P., 1992, Numerical recipes in FORTRAN. The art of scientific computing. Cambridge University Press

Raghavan D., McAlister H. A., Henry T. J., Latham D. W., Marcy G. W., Mason B. D., Gies D. R., White R. J., ten Brummelaar T. A., 2010, ApJS, 190, 1

Rauscher E., Menou K., 2012, ApJ, 750, 96

Seager S., Mallén-Ornelas G., 2003, ApJ, 585, 1038

Seager S., Sasselov D. D., 2000, ApJ, 537, 916

Southworth J., 2009, MNRAS, 394, 272

Southworth J., 2010, MNRAS, 408, 1689

Southworth J., 2011, MNRAS, 417, 2166

Southworth J., Hinse T. C., Dominik M., Glitrup M., Jørgensen U. G., et al. 2009, ApJ, 707, 167

Spiegel D. S., Burrows A., 2010, ApJ, 722, 871

Stetson P. B., 1987, PASP, 99, 191

Stevenson K. B., Harrington J., Fortney J. J., Loredo T. J., Hardy R. A., Nymeyer S., Bowman W. C., Cubillos P., Bowman M. O., Hardin M., 2012, ApJ, 754, 136

Torres G., Andersen J., Giménez A., 2010, A&A Rev., 18, 67

Triaud A. H. M. J., Collier Cameron A., Queloz D., Anderson D. R., Gillon M., Hebb L., Hellier C., Loeillet B., Maxted P. F. L., Mayor M., Pepe F., Pollacco D., Ségransan D., Smalley B., Udry S., West R. G., Wheatley P. J., 2010, A&A, 524, A25+

van Leeuwen F., 2007, A&A, 474, 653